Impact of Background Oxygen Pressure on the Pulsed-Laser Deposition of ZnO Nanolayers and on Their Corresponding Performance as Electron Acceptors in PbS Quantum-Dot Solar Cells

Qian Dong,[†] Huiyan Liu,[‡] Yukihiro Hara,[§] Hannah E. Starr,[⊥] Jillian L. Dempsey,[⊥] and Rene Lopez*[,†,‡,§]

[†]Department of Applied Physical Sciences, [§]Department of Physics and Astronomy, and [⊥]Department of Chemistry, University of North Carolina at Chapel Hill, Chapel Hill, North Carolina 27599, United States

[‡]School of Physical Science and Technology, Shanghai Tech University, 393 Middle Huaxia Road, Shanghai 201210, China

ABSTRACT: ZnO films are commonly employed as n-type semiconductors in heterojunctions with PbS colloidal quantum-dot (CQDs) films because of their outstanding optical transparency and electron acceptor properties, yet studies of the impact of ZnO film microstructure, composition, and defect qualities on the solar-cell performance are quite limited. Here we report on the fabrication of ZnO films via pulsed-laser deposition and use these films to investigate how different morphologies affect the PbS CQD solar-cell performance. By modification of the background gas O_2 pressures during the ZnO deposition process, the device performance approaching a 7.8% energy conversion efficiency is achieved with an O_2 pressure of 100 mTorr. Higher or lower O_2 pressures led to significantly lower device efficiency. We employ various materials and device characterizations to highlight the differences in the physical properties introduced by the fabrication oxygen pressure. In particular, we have found that the differences in the type and density of ZnO oxygen defects are the key factors behind the dispersion in solar-cell performances.

KEYWORDS: ZnO, PbS quantum dots, thin-film solar cell, physical mechanism, pulsed-laser deposition
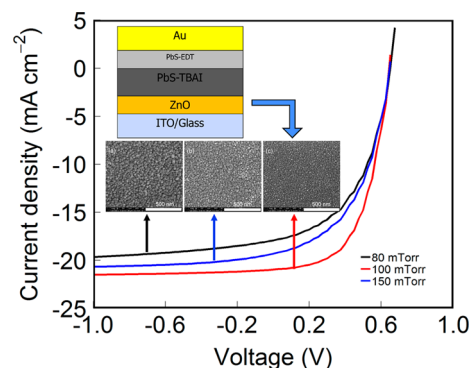
INTRODUCTION

PbS and PbSe semiconducting colloidal quantum dots (CQDs) have been widely investigated because of their wide range of optoelectronic device applications such as photovoltaic devices,[1−4] photodetectors,[5] and light-emitting diodes.[6−8] The extensive attention of CQDs by researchers originates not only from their unique properties such as tunable band gap via particle-size modification[9−11] and convenient energy-level adjustment via molecular linkers[12,13] but also from their practical device fabrication advantages, such as the ease of operation of solution-based processing at low temperature and low cost. Specific to solar cell applications, the significant developments in CQD solar cells have been mainly realized through two routes: device architecture engineering and surface passivation. Through those, the highest reported certified power conversion efficiency (PCE) of 12% was recently achieved.[14] Additionally, PbS CQD solar cells with different architectures have been reported with outstanding air stability.[4,15−17]

Among the numerous studies of the depleted-heterojunction CQD solar-cell performance improvements, the majority of researchers have devoted their attention to optimization of the absorbing layer. The exploration of window-layer materials is rather limited even though they play a crucial role in the extraction and transportation of the charge carriers. It has already been demonstrated that ZnO is an excellent candidate as an electron-transport layer because it possesses relatively high mobility, high optical transparency (wide band gap), abundance, and ease of fabrication and processing.[18,19] The excellent photosensitive response of ZnO to ultraviolet (UV) radiation is also well-known and adds to its utility in solar cells.[20] Several groups have explored various modifications to ZnO films and monitored the effect of these modifications in solar cells to achieve >8% PCE.[4,16,21,22] Song and Cheng's group, for instance, studied the impact of different ZnO thicknesses on optimization of the CQD solar-cell performance.[23] Until a few years ago, nanowires of ZnO, which deviated from common flat architectures, were considered to be an enabler architecture that eased the transport of electrons out of the CQD layer. For example, Bawendi, Gradečak, and co-workers[24,25] fabricated ZnO nanowire arrays to improve the solar-cell device performance with large photocurrents. Nevertheless, the most efficient ZnO CQD solar cells reported have employed flat films, but the impact of the ZnO film

microstructure on optimization of the CQD solar-cell performance still requires further investigation because some morphological variations, optimized by just the final device performance, are not particularly well understood.

To investigate the effect of different ZnO film morphologies, covering not just microstructure but composition and defects, a suitable fabrication method must be considered. Because of its simplicity and large-area applicability, sol−gel is more commonly used to deposit ZnO in order to study the CQD photovoltaic devices.[26−28] However, sol−gel approaches typically only allow easy adjustment of the film thickness, making additional film morphology control a challenge. Therefore, it is imperative to find an alternative way to make this morphology control be practicable. Pulsed-laser deposition (PLD) is a method for ZnO film fabrication by which researchers have reported that one can tailor subtle changes in the film surface morphology and properties via its deposition background gas pressure.[29,30] Inspired by this, in this work we employ PLD with various oxygen gas pressures to obtain ZnO films with different microstructures and examine the performances of the corresponding ZnO−PbS CQDs photovoltaic devices. Although oxygen pressure increases during PLD fabrication produced monotonic trends in the grain size, crystallinity, and electron mobility, once these ZnO layers were incorporated into PbS CQD solar cells, the photovoltaics showed a peak in the performance at the midpressure fabrication setting. Investigation of the underlying physical mechanism showed that such a midpressure enhancement arises from a reduction in the bimolecular recombination, which we trace to an enhancement in the carrier lifetime and a minimization of the ZnO oxygen defect densities. Our experimental data demonstrate a detailed information on how to obtain an optimal morphology for the ZnO film to improve the device performance and reveal that simple crystallinity or grain enhancement is insufficient. Moreover, our work provides clear guidance on the minimal quality and morphology that the electron-transport layer must possess for the successful fabrication of heterojunction oxide−PbS CQD-based solar cells.

■ RESULTS AND DISCUSSION

Considering the architecture of the solar cells, the most obvious role the ZnO-based entry window should play is to provide an n-type electrical layer with minimal impedance for light transmittance into the absorbing layer. The UV−vis spectra of three types of ZnO films that were deposited under different oxygen gas pressures are shown in Figure 1. To make it simple, before further discussion, we designate the ZnO film deposited under 80 mTorr oxygen as type I ZnO, under 100 mTorr oxygen as type II ZnO, and under 150 mTorr oxygen as type III ZnO. Notably, all of the curves present a clear UV absorption edge around 375 nm wavelength and a large transmission (80−90%) from the blue to near-IR wavelength region. However, the curves are not identical, and we can see that the high transmission region presents a modulation typical of interference effects across the oxide layer. Ellipsometry measurements show that the ZnO index of refraction decreases slightly under increased oxygen pressure. The refractive indices for the 80, 100, and 150 mTorr films are 1.89, 1.82, and 1.78, respectively (taking the 500 nm wavelength value as representative of the visible range). This optical change (compared with the bulk ZnO index at 500 nm wavelength, which is 1.98) may arise from the structural changes in the
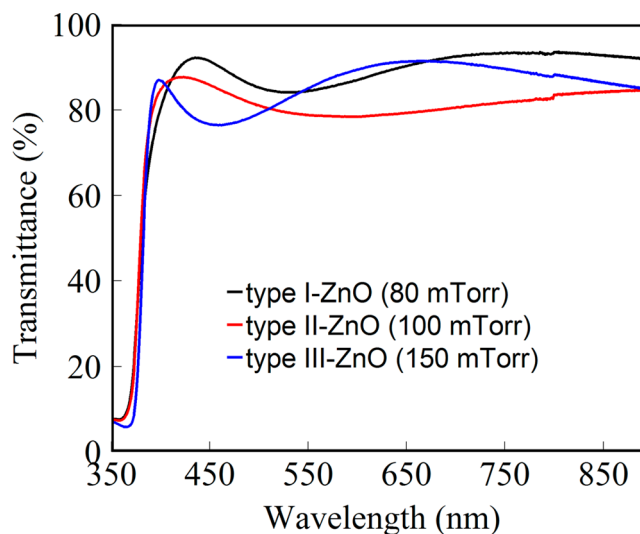

Figure 1. Optical transmission spectra of three different types of ZnO films.

film. This is confirmed by inspection of the scanning electron microscopy (SEM) micrographs of the ZnO films prepared at various oxygen pressures. As indicated in Figure 2, an inverse relationship between the oxygen pressure and the grain size of the ZnO film is an obvious effect. Less obvious, but in association with the index of the refraction drop, the grains are not only smaller but also less densely packed. This effect from PLD has been shown in other instances.[31] The results from atomic force microscopy (AFM) analysis (Figure S1 in Supporting Information) agree well with the SEM results. They reveal that the root-mean-square roughness in the films increases along with and increase of the background gas pressure, forming a progressively less compact microstructure composed of smaller nanocrystallites.

This microstructural change is coupled with structural quality changes on the atomic scale. To explore this connection, we perform X-ray diffraction (XRD) to analyze the crystal structures of the deposited ZnO films (Figure S2). The XRD patterns of the three types of ZnO films indicate that they present the expected wurtzite structure, but as can be noted, the C-axis-oriented (002) peak intensity decreased significantly following the oxygen pressure increase, with a concomitant increase of the full width at half-maximum (fwhm). Scherrer's[32] relationship between the X-ray line sharpness and size of the nanocrystallites confirms the microstructural changes that we already noted from the SEM micrographs. The XRD data have a more important implication, specifically that the smaller crystallites are also increasingly incoherently connected (breaking crystal translation symmetry) among each other. Thus, although the film morphologies and their optical properties are quite similar, we could expect that the microstructure qualities will have a marked influence in the electron-transport properties, namely the carrier-transport mobility.

The field-effect transistors (FETs) with the ZnO film in the channel are fabricated to study the electrical transport properties of the ZnO films prepared at different pressures.[33] The detailed electrical parameters obtained from FET measurements are summarized in Table 1. We observe that the carrier mobility of the ZnO films decrease while increasing the oxygen gas pressure during deposition. Simultaneously, the
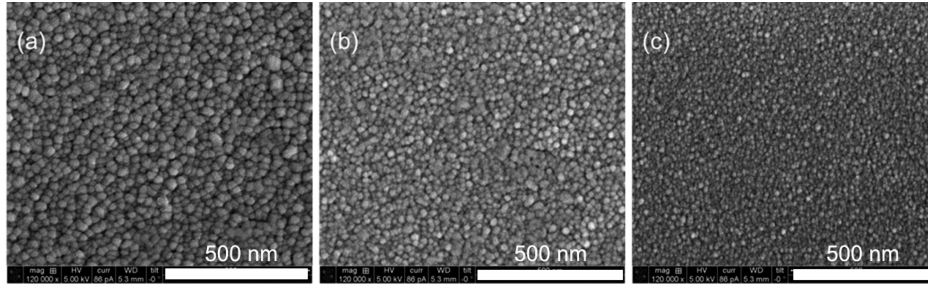
Figure 2. SEM images of the deposited ZnO films under different oxygen pressures: (a) 80 mTorr; (b) 100 mTorr; (c) 150 mTorr.

Table 1. Deposition Oxygen-Pressure-Dependent Electrical Properties for Different ZnO Films

deposition oxygen pressure (mTorr)	carrier concentration (cm^{-3})	mobility $(cm^2\ V^{-1}\ s^{-1})$	conductivity $(S\ cm^{-1})$
80	2.9×10^{14}	5.1	1.6×10^{-4}
100	6.5×10^{14}	3.4	5.3×10^{-4}
150	1.5×10^{16}	2.4	5.6×10^{-3}

correlated carrier concentrations increase. The ZnO film deposited under lower oxygen gas pressure gives a larger carrier mobility owing to the smaller number of grain boundaries in such a film,[30] as observed in the SEM images (Figure 2). Overall, the trends in the optical transmission, SEM, AFM, XRD, and mobility data indicate that the ZnO film fabricated with the lowest oxygen pressure has the best morphology and electronic properties. However, as shown below, subsequent studies of solar cells fabricated with these films revealed that these trends do not correlate with the solar-cell performance.

Solar-cell devices were fabricated in a layered structure with ZnO/PbS-TBAI/PbS-EDT/Au (TBAI = tetrabutylammonium iodide; EDT = 1,2-ethanedithiol) on an indium−tin oxide (ITO)/glass substrate (schematic in Figure 3a). Each
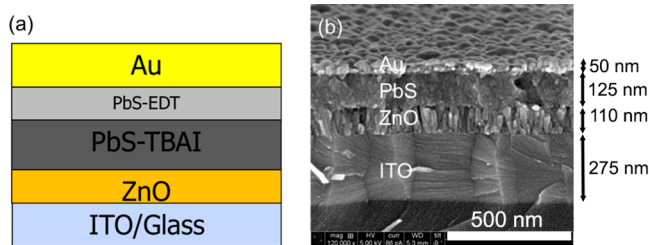

Figure 3. (a) Schematic device structure showing the heterojunction between n-type ZnO and p-type PbS CQDs. (b) SEM cross-sectional image of type II ZnO−PbS CQD devices indicating layer thicknesses.

particular layer was created as described in detail in the Methods section and with thicknesses within 5% of those shown in the representative example in Figure 3b. It is worth pointing out that, for the three types of ZnO films, the film thicknesses are 108 ± 1, 110 ± 1, and 113 ± 1 nm, respectively. Because the thickness difference is still within 5%, its influence on the device performances could be ignored, and we approximately take the film thicknesses for all types as the same. The current−voltage (J−V) characteristics and external quantum efficiency (EQE) spectra of the three types of ZnO−PbS CQD solar cells are displayed in Figure 4a. The typical devices with type I ZnO exhibited a J_{SC} of 17.3 mA cm^{-2}, a

V_{OC} of 0.64 V, and a fill factor (FF) of 48.2%, resulting in a PCE of 5.3%. Fabricated at 100 mTorr of oxygen, the type II ZnO devices surprisingly presented a significant PCE enhancement, delivering a local champion device (type II ZnO) with a PCE of 7.4% and a J_{SC} of 21.1 mA cm^{-2}. However, when the oxygen pressure was further increased to 150 mTorr (type III ZnO), the PCE of the devices suffered a substantial deterioration. The descriptions of the ZnO films and the corresponding device performance parameters are listed in Table 2 in detail. Comparing the different devices, we can see that both J_{SC} and FF of type II ZnO are simultaneously improved with very minimal changes in V_{OC}. This is confirmed by the ultraviolet photoelectron spectroscopy (UPS) measurements on ZnO films deposited under different oxygen pressures (Figure S3). With an increase of the oxygen gas pressure, the Fermi level regarding the vacuum did not show an obvious change, indicating that a similar V_{OC} can be expected for the devices with different types of ZnO films. In order to guarantee that this was not an anecdotical event in the device performance, 20 devices of each type were tested. The statistical deviations from the median values are relatively small (under 7% variation) for all devices, supporting the conclusion that ZnO morphological changes induced by the PLD oxygen pressure are indeed behind this substantial solar-cell performance effect. Still though, as highlighted above, this solar performance trend does not simply follow the SEM/AFM/XRD structural tendencies or the electrical parameters derived from the ZnO FETs characterization.

To identify the origin of the J_{SC} improvement, we obtained the EQE spectra for different types of ZnO-film-based PbS CQD solar cells, as shown in Figure 4b. In order to make comprehensive comparisons, the EQE spectra are divided into three distinctive regions. In the UV region (400−450 nm), the higher EQE value in type I ZnO devices is consistent with the outcome of the optical transmission spectrum discussed above. This optical difference is not large, but it might explain the slight relative decrease for both type II ZnO- and type III ZnO-based devices. In the visible region (450−700 nm), the EQE of type II ZnO devices demonstrates a higher, broader, and more feature-rich response, which states that type II ZnO devices couple to visible wavelengths more effectively and/or could more efficiently extract the charge carriers. In the IR region, the EQE spectra overlap quite well for all three types of devices, and this confirms, as others have demonstrated, the positive role of the PbS-TBAI/PbS-EDT back structure to secure the IR-originated carriers' extraction.[4] On the basis of these observations, it is clear that the higher J_{SC} of type II ZnO devices is attributed to improvement of the EQE in the visible region. However, the significant change in the FF indicates that this is not a pure optical enhancement arising from a
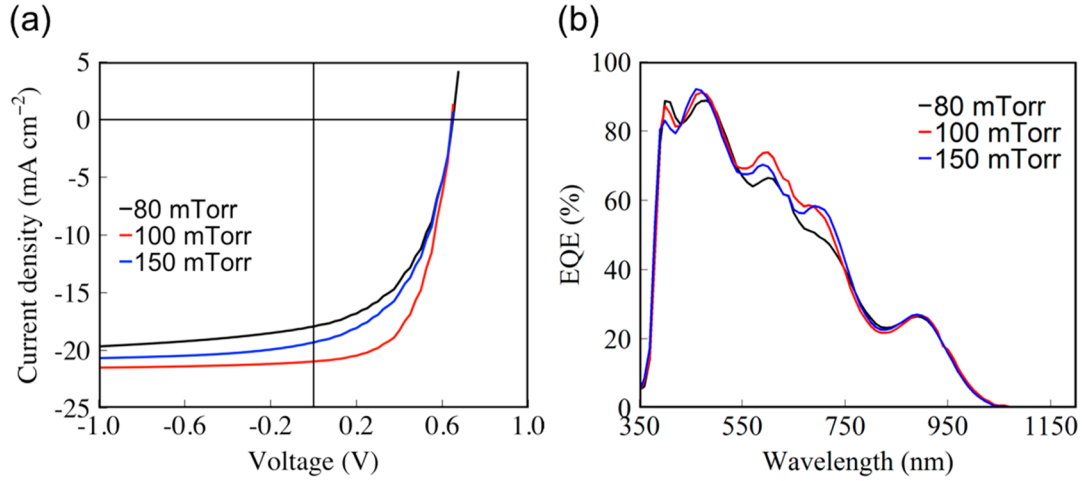
Figure 4. (a) Representative $J-V$ characteristics. (b) EQE curve of devices with ZnO films under different deposition oxygen pressures.

Table 2. Performance Parameters of Three Types of Devices Summarized from Figure 4

device	V_{OC} (V)	J_{SC} (mA cm^{-2})	FF (%)	PCE (%)
Type I ZnO−PbS device (80 mTorr)	0.64 ± 0.01	17.2 ± 0.7	48.2 ± 0.5	5.3 ± 0.2
Type II ZnO−PbS device (100 mTorr)	0.64 ± 0.01	21.1 ± 0.1	55.6 ± 0.1	7.4 ± 0.3
Type III ZnO−PbS device (150 mTorr)	0.64 ± 0.01	19.3 ± 0.2	48.7 ± 0.1	6.0 ± 0.2

constructive light-interference event originating of the film thickness and index of refraction combination of the whole stack. Indeed, the $J-V$ curve shows that at high reverse bias (−1 V) all of the current densities closely converge ∼20−21.5 mA cm^{-2}, indicating that the optical differences are not substantial enough to explain the behavior from the short circuit to the forward bias regions.

To identify the fundamental reasons behind the performance differences between different types of devices, the $J-V$ characteristics and EQE spectra under various illumination conditions were performed to explore the charge carriers' recombination process. The charge collection probabilities of the devices under various light intensities are obtained by manipulating the $J-V$ characteristics and from which the predominant recombination mechanism (bimolecular/monomolecular recombination) is recognized. As discussed in other literature reports,[34−36] the photocurrent of a PbS CQD-based solar cell with a thickness z of the PbS film could be derived from a simplified model of charge generation/collection:

$$J_{ph} = e \int G(LI) \, P_c(LI,V) \, dz \tag{1}$$

where $G(LI)$ is the absorbed photon flux per unit volume and $P_c(LI,V)$ is the probability of charge collection [G is a function of the light intensity (LI) and P_c is left to possibly be].[34−36] Alternatively, under a more common situation in which we do not consider the effect of the device geometry, this probability can be presented as

$$P_c(LI, V) = |J_{ph}(LI, V)/(J_{ph} \text{ at saturation})| \tag{2}$$

Given that the saturated current is set at −1 V for all three kinds of devices, we could expand the collection probability as follows:

$$P_c(LI, V) = |J_{ph}(LI, V)/J_{ph}(LI, -1V)| \tag{3}$$

As shown in Figure 5, under different light intensities, the charge collection probabilities derived from the equations discussed above do not overlap exactly at all applied voltage biases for all three types of devices. This is a qualitative indication of the existence of bimolecular recombination[34−36] for all three device types, but the curves also indicate that its prominence in each device type is significantly distinct. In the type II device, the normalized curves overlap quite well in the reverse bias region and their degrees of dispersion over the positive voltage range are relative smaller. In sharp contrast, for both the type I and III devices, all of the curves start to disperse immediately from the reverse bias region. The curves dispersion for the type I device is the widest, even more than that for the type III device, especially in the reverse bias region. Therefore, this demonstrates that bimolecular recombination appears significantly greater in both the type I and III devices. This is the most likely physical reason accounting for the reduction in the FF compared to the type II device.

Figure 6 shows the EQE spectra measured while the devices were exposed to different white-light intensities (all taken in short-circuit conditions). In an ideal case, the EQE dark curve should overlap well with that under extra white-light exposure. In other words, as before, the more acute EQE curve dispersion indicates that more recombination is occurring under illumination. When the three types of devices are compared, the EQE curve of the type II device shows the least dispersity versus the dark curve through the whole wavelength region.

The above light-intensity experiments all confirm that the differences in bimolecular recombination are the key factor separating the performance between devices. However, how is this type of recombination linked to the ZnO fabrication differences? In order to make headway in this key question, we have directed our attention to quantitatively studying the charge-carrier accumulation and transport in the PbS CQD-based solar cells. Electrochemical impedance spectroscopy (EIS) is a very powerful tool for the investigation of the impedance spectra of these devices under different V_{OC} conditions that were extracted from the $J-V$ characteristics
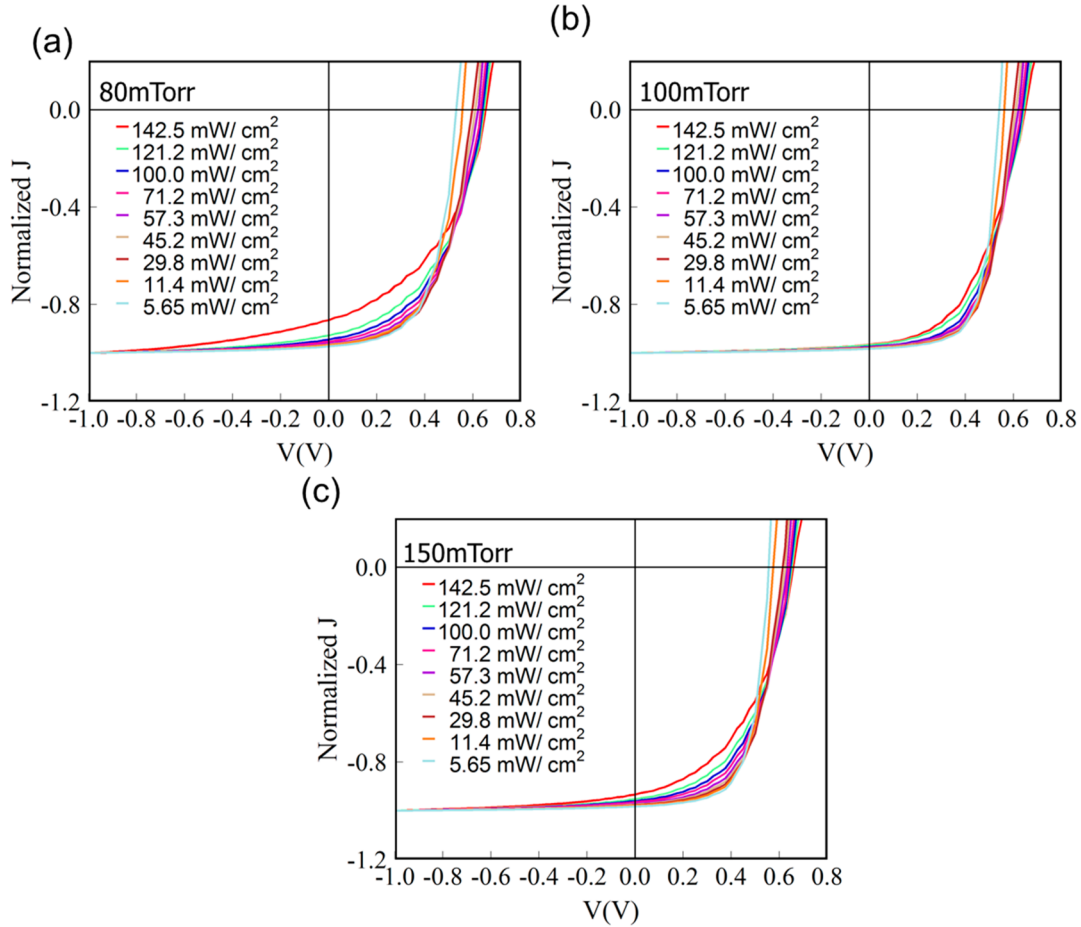
Figure 5. Charge collection probabilities of the devices with ZnO films under different deposition oxygen pressures: (a) 80 mTorr; (b) 100 mTorr; (c) 150 mTorr. The charge collection probabilities of all are derived from the normalization of their $J-V$ characteristics under different light intensities, respectively.

induced under different light intensities (Figure 7). In these curves, Z, the complex impedance of the device is expressed by the two parts, the real part Z' and the imaginary part Z''. The relationship among those three is shown as follows (eq 4):

$$Z(\omega) = Z' + iZ'' \tag{4}$$

The frequency is an indirect parameter in Figure 7, and it decreases along the semiarc from left to right under different light intensities.[37,38] Although the semiarcs look quite similar, quantitatively there are important differences. In the low-frequency region, the recombination resistance is quantified by the value derived from the cross point of the EIS curve and the Z' axis.[38,39] In Figure 8a, we show these recombination resistances versus V_{OC} obtained under different light bias conditions. A large recombination resistance (R_{rec}) is a necessary element for high-performance PbS CQD-based solar cells because the accumulated charge carriers are allowed to flow through the external circuit under this circumstance.[38,40] EIS also allowed us to characterize the carrier lifetime of these CQD-based solar cells. This is a crucial parameter to describe the charge dynamics of the solar cells. Generally, the primary relaxation process could be expressed by the following equation:[38,41]

$$I(t) = Ae^{-t/\tau_1} \tag{5}$$

where A is a constant, τ_1 is the carriers' lifetime, and t is the time. The relaxation process listed above can be associated

with a characteristic frequency,[38,42] which is simply given in the following equation:

$$\omega_1 = 1/\tau_1 \tag{6}$$

where the value of the frequency ω_1 can be directly derived from the plot of the imaginary part of the impedance Z'' as a function of the frequency. ω_1 is the frequency that corresponds to the peak value of Z''. In Figure 8b, it is clear that the lifetime of the carriers in a type II device is the longest among the three types of devices, followed by type III and type I under illumination.

Up to this point, we can partially summarize the findings by stating that the differences in the solar-cell performance are due to different rates of bimolecular recombination, and this deleterious effect is minimal in type II ZnO-containing solar cells because its carrier lifetime and recombination resistance are the largest. Because the only difference in these devices is in the ZnO morphology, we should be able to connect the improved device metrics to the type II ZnO structural/compositional morphological characteristics.

However, given that the mobility and charge lifetime should be positively correlated, why does the FET mobility characterization not anticipate the EIS observations? We believe the most important reason behind this apparent discrepancy is that the FET measures transport qualities in-plane along the film surface but not across the film-thickness dimension, the way charges move in solar-cell operation and are actually probed by
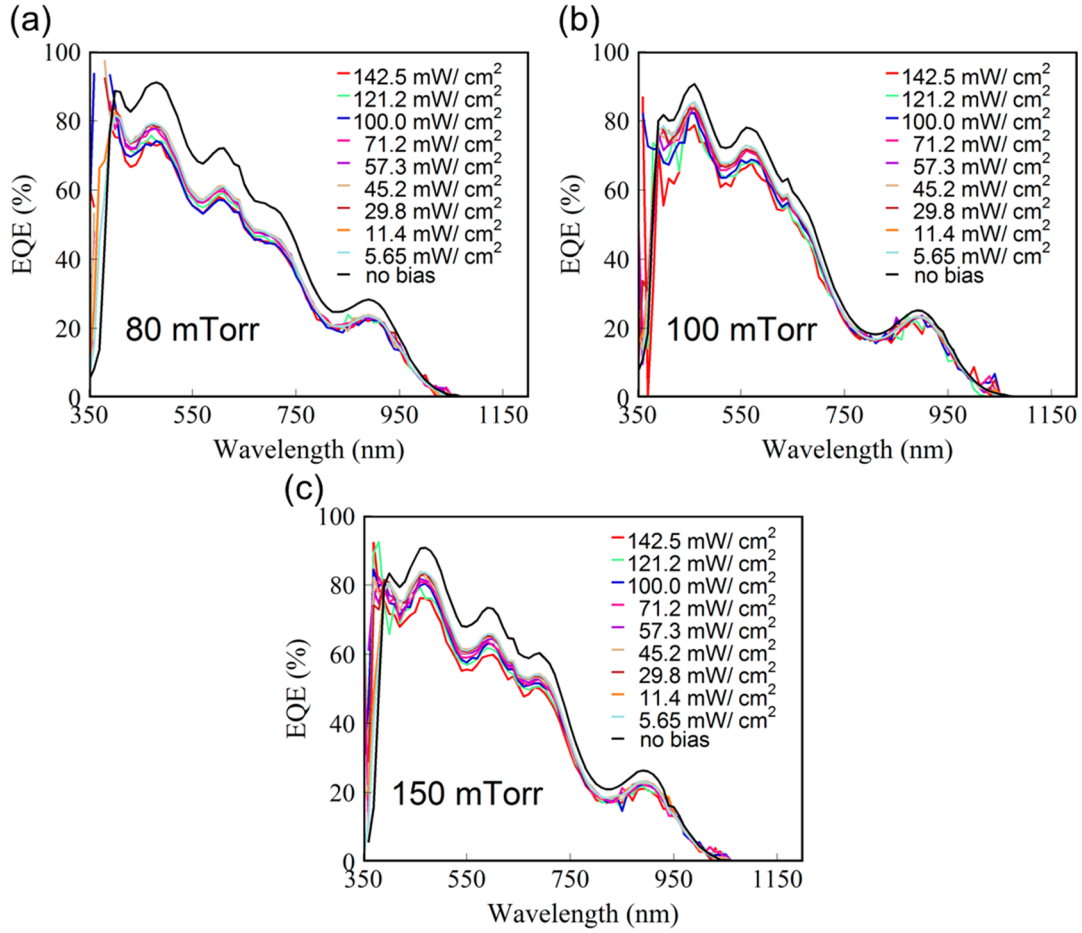
Figure 6. White-light bias EQE spectra of the devices with ZnO films under different deposition oxygen pressures: (a) 80 mTorr; (b) 100 mTorr; (c) 150 mTorr.

EIS. As shown in the SEM micrographs, the structures of the films are granular but are also somewhat columnar (Figure 2); thus, defects in-plane across those columns are likely to affect the FET measured mobilities, but the defects along the film thickness likely play a larger role in solar-cell operation.

To probe the existence and density of defects in the ZnO layers, we have employed several approaches, the first of which is transient photovoltage spectroscopy.[43,44] Using this technique, the trap state densities of the three types of devices have been explored. For an ideal trap-free semiconductor, the photogenerated electrons under illumination experience a very fast relaxation process to the conduction band edges and still sustain dynamic thermal equilibrium. This situation is applicable for the holes in the valence band. The two quasi-Fermi levels that they establish are directly corresponding to the V_{OC} itself. For a semiconductor with traps, upon illumination some of the photogenerated carriers are used to fill the traps and therefore generate a smaller V_{OC}. This process could be revealed with transient photovoltage spectroscopy. On top of a constant light bias, a 532 nm nanosecond laser was employed for the V_{OC} modulation. Parts a−c of Figure 9 show the capacitance, carrier concentration (n), and density of trap states (DOS) at a series of V_{OC} values. Given the assumption that the exciton generation and applied bias are noncorrelated and a small recombination occurs under short-circuit conditions, because the capacitance corresponds to the stored charge in the bulk of the film, a larger capacitance implies more trap states in the film. Here n can also be seen as the number of

extra carriers used for separation of the quasi-Fermi levels and V_{OC} accordingly (more details on this method can be found in ref 1). As shown in Figure 9, in all parameters n, capacitance per unit area, and particularly the DOS, the lowest values are all associated with the type II device, followed by the type III device, and the highest are in type I. This is consistent with the photovoltaic performance shown earlier. We note that this technique cannot distinguish where the defects are located. Because ZnO is the electron acceptor, we presume that some defects are at energy states below the conduction band in ZnO, but some may also exist within the PbS layer. However, as noted earlier, extreme care was taken to ensure uniformity in the PbS layer across samples so that most differences can be attributed to ZnO itself.

On the basis of the aforementioned results and discussion, the performance improvement with optimized ZnO film morphology can now be thoroughly explained. Despite showing a better planar mobility, presumably because of its in-plane compactness, type I ZnO has a higher overall density of defects. The best cell performance obtained from type II ZnO arises because it presents the lowest defect DOS, the largest carrier lifetime, and thus a reduced bimolecular recombination.

Finally, what physical defects have been caused by the ZnO performance disparity? Photoluminescence (PL) and X-ray photoelectron spectroscopy (XPS) were employed to bring light to this last question. Figure 10 shows the PL and XPS spectra for the three different types of ZnO films. As illustrated
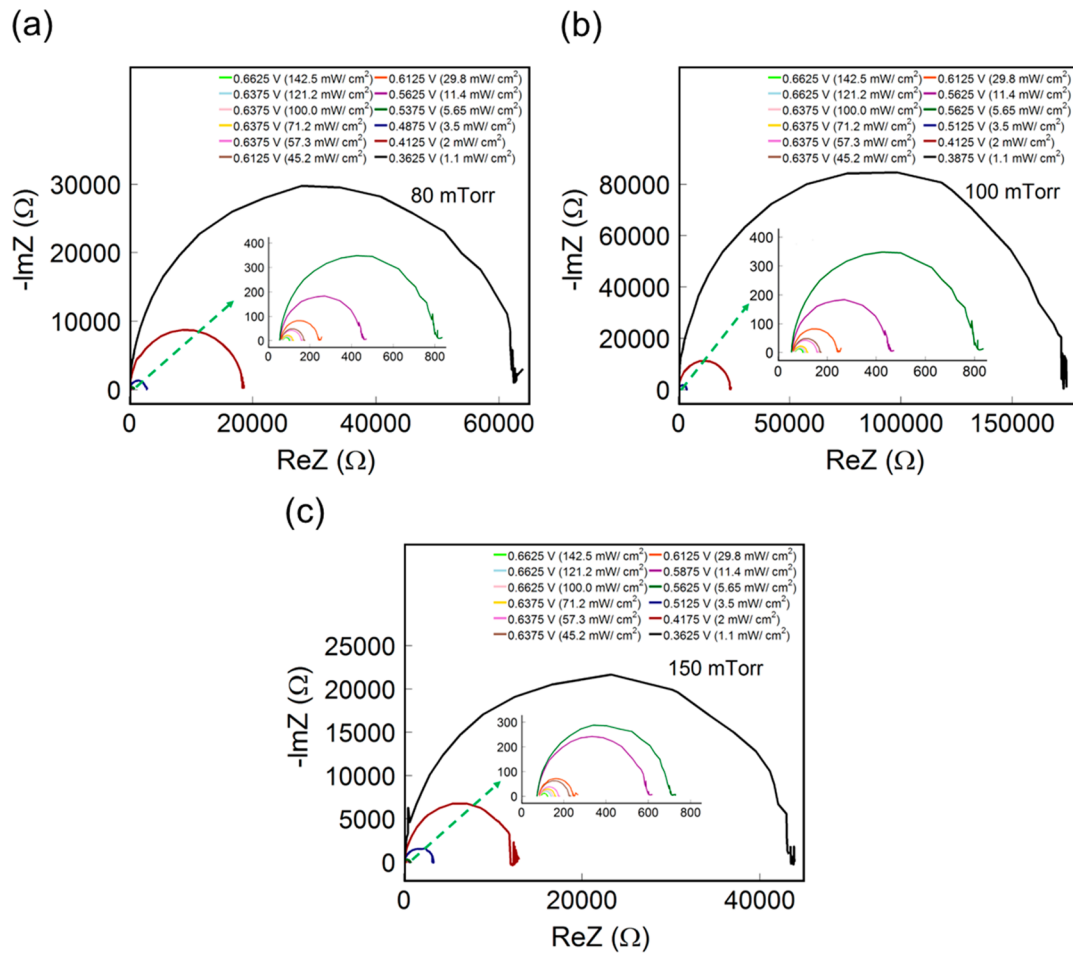
Figure 7. Impedance spectra for the devices with ZnO films under different deposition oxygen pressures: (a) 80 mTorr; (b) 100 mTorr; (c) 150 mTorr.
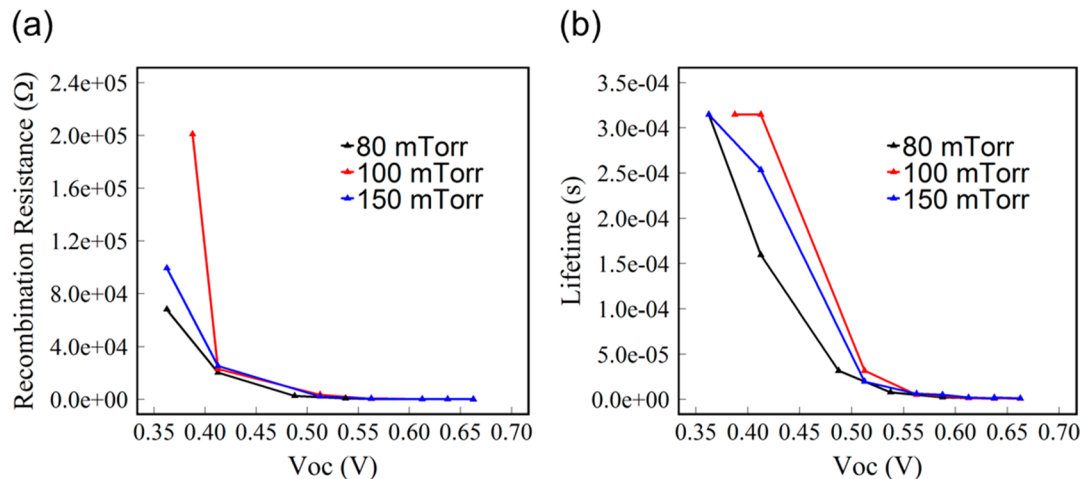

Figure 8. (a) Recombination resistance and (b) carrier lifetimes for the devices with ZnO films deposited under different oxygen pressures.

in the PL spectra (Figure 10a), the two emission peaks indicate different kinds of emissions. The band-edge emission is indicated by the peak centered near 400 nm, and the oxygen vacancy (V_O) defect-related emission, in turn, is indicated by the other broad one centered at 660 nm.[45−47] Among the three types of ZnO films, type I ZnO has the highest peak related to the V_O defect, which is likely the ultimate culprit behind its lower performance in the solar cells. This is also the most likely

reason for the device's slight EQE losses within the 500−800 nm wavelength region in absorption/emission. On the other hand, XPS analysis provides details on the state of the surface oxygen ions in ZnO. As shown in Figure 10b−d, the deconvoluted oxygen binding peak for ZnO could be expressed by two contributing signals: the lower-binding-energy peak (529.2 eV) corresponds to the oxygen atoms in a ZnO matrix, and the higher-binding-energy peak (531.5 eV) corresponds to
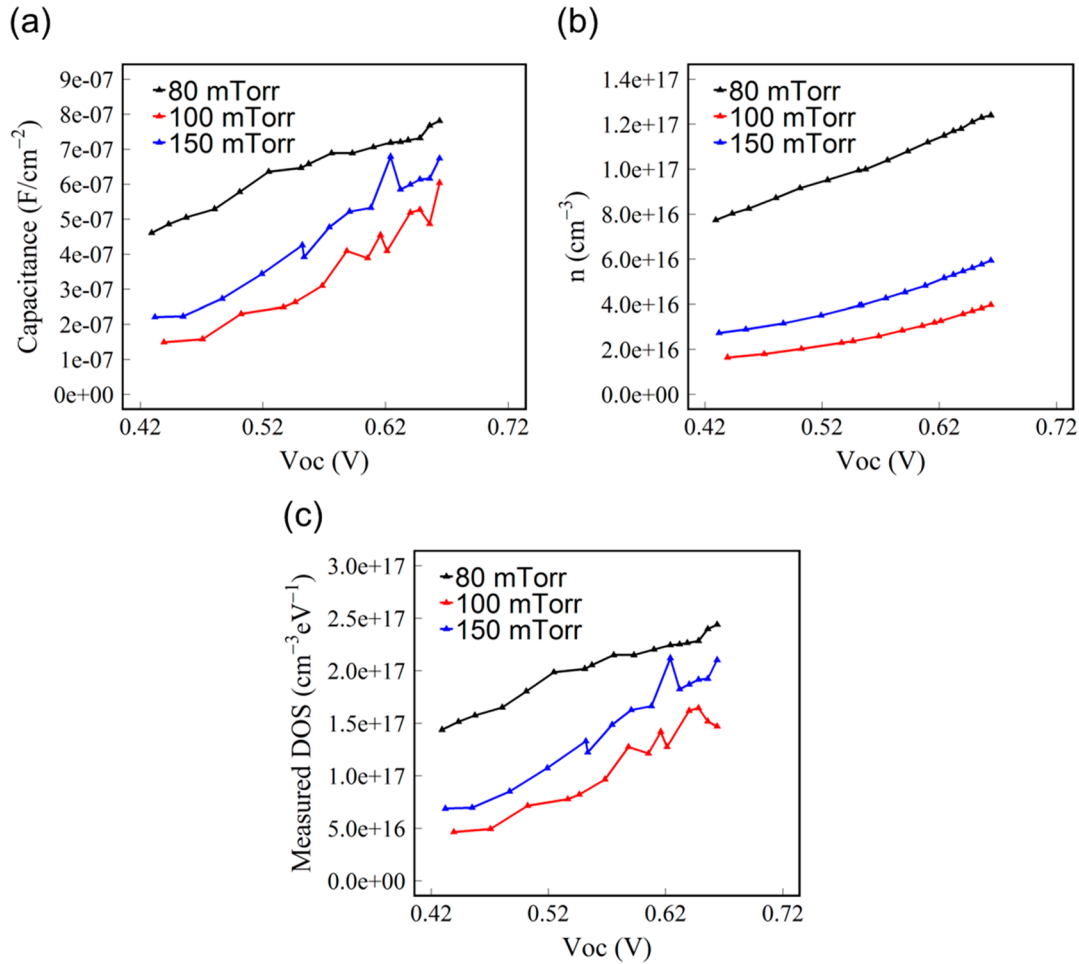
Figure 9. Capacitance (a), carrier concentration (b), and DOS (c) for the devices with ZnO films deposited under different oxygen pressures.

the oxygen interstitial defects.[48] The numbers shown within the figure are the ratios of the area of the lower-binding-energy peak to that of the higher-binding-energy peak, which indicate the relative content of the oxygen-defected binding sites in the ZnO film. The data in Figure 10b,c show the relatively smaller intensities of the higher-binding-energy components, indicating that the oxygen interstitial binding defects in the ZnO films are lower at the two lower oxygen fabrication pressures. These XPS and PL results indicate that the decline of the vacancies and the rise of the oxygen interstitials along the oxygen pressure increase the path, introduce different traps, and hinder the mechanisms to charge transport in the solar cell. The best morphology of the ZnO film thus seems to result from a balancing act between these compositional layer defects.

■ CONCLUSION

During the fabrication of three types of ZnO films by PLD, which differed only in the oxygen pressures employed during growth, we encountered very distinct differences that had a remarkable impact on their performance as part of PbS CQD solar cells. Oxygen pressure increases led to small grain sizes, less crystallographic alignment, lower film density, and a decreased index of refraction, which, in turn, resulted in a decreasing in-plane electron mobility. Notwithstanding this monotonic trend, the midfabrication pressure, 100 mTorr, actually resulted in the higher PCE performance of 7.8%, due to significantly enhanced J_{SC} and FF relative to the devices with

ZnO made at the highest and lowest fabrication pressures. Light and voltage bias analyses showed that the bulk of this improvement originated from limited bimolecular recombination, which was likely a consequence of an extended carrier lifetime and a relatively low defect density. The defects are not limited to one defect type; rather there are the luminescent defects associated with oxygen vacancies declining with oxygen fabrication pressure and other types associated with interstitial/amorphous ZnO. These results highlight the clear morphology changes that a single processing variable can induce to modify the microstructure and atomic structure of the material and thereby lead to drastic optoelectronic property changes. Direct measurement of the material defect types and densities might be no less important than more immediate characterizations such as the crystallinity, grain size, or even in-plane mobility. Further work is now directed toward determining whether the ZnO oxygen defects are a bulk-transport hindering factor or only possibly acting at the interface with the PbS CQD film.

■ METHODS

Materials. Lead(II) oxide (99.999%), anhydrous hexane (95%), tetrabutylammonium iodide (TBAI; >99%), 1-octadecene (95.0%), hexamethyldisilathiane (synthesis grade), 1,2-ethanedithiol (EDT, 99%), oleic acid (99%), anhydrous acetonitrile, and methanol were acquired from the chemical company Sigma-Aldrich.
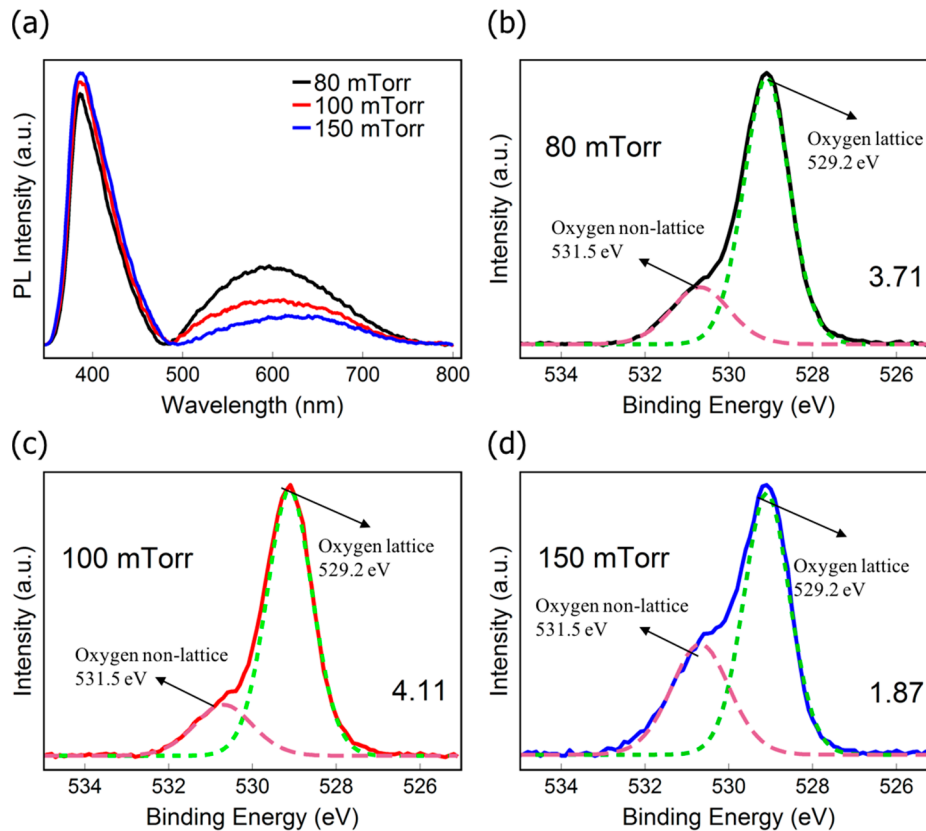
Figure 10. (a) Steady-state PL spectra of ZnO films with different morphologies. Deconvoluted XPS spectra of the O 1s core level of ZnO films under different deposition oxygen pressures: (b) 80 mTorr; (c) 100 mTorr; (d) 150 mTorr. The numbers shown within the figure are the ratios of the area of the lower-binding-energy peak to that of the higher-binding-energy peak, which indicate the relative content of the oxygen-defected binding sites in the ZnO film.

Synthesis of PbS CQDs. PbS CQDs were synthesized via a modified version of the procedure of Hines et al.[49−51] The description of the synthesis procedures is included in the Supporting Information.

Synthesis of the ZnO Film. The ZnO film was prepared by PLD. ITO-coated glass was ultrasonically washed successively in a detergent, deionized water, acetone, and isopropyl alcohol and then dried under air. ZnO films were deposited on clean ITO glass by PLD (PVD Products Nano-PLD-1000 Pulsed Laser Deposition System, configured with a 248 nm KrF excimer laser) at room temperature from a ZnO target (Kurt J. Lesker 99.9% purity). The oxygen gas pressure was set as 80, 100, or 150 mTorr, and the flow rate was set as 5 sccm. The chamber was pumped down to 10^{-6} Torr before flowing the oxygen and starting the ZnO deposition. For ZnO film deposition, a pulse energy of 200 mJ and a repetition rate of 40 Hz were used. All ZnO films were then annealed in air for 30 min at 350 °C.

Fabrication of the Solar Cells. PbS CQD films were fabricated through solid-state ligand exchange via a layer-by-layer dip-coating technique, and the whole process was conducted in air. Each cell was composed of 35 layers of TBAI-coated PbS CQDs and 5 layers of EDT-coated PbS CQDs. For the preparation of one layer of TBAI-coated PbS, substrates were dipped in four different solutions successively: (1) a TBAI (10 mg mL^{-1} in methanol) solution was used as the linker solution, (2) a 7.5 mg mL^{-1} PbS CQD solution was used in hexane, (3) a TBAI (10 mg mL^{-1} in methanol) solution was used as an exchange solution, and (4) methanol was used as a rinsing solution. For each solution, the substrates were immersed for 5, 20, 15, and 5 s and withdrawn at speeds of 1, 10, 10, and 10 mm s^{-1} followed by drying times of 60 s, 80 s, 30 s, and 60 s, respectively. The same dip-coating process parameters and sequences were applied for the subsequent preparation of layers of EDT-coated PbS films with a EDT solution (0.02% by volume in acetonitrile). A total of 100 nm of gold was used as the photocathode, and it was deposited in a thermal evaporator under 10^{-6} mbar.

Characterization of the ZnO Film. X-ray diffraction (XRD) with a Cu Kα X-ray emission line (Rigaku Multiflex X-ray diffractometer) was performed to characterize the crystal structure, and atomic force microscopy (AFM; USA Bruker, Dimension Icon/FastScan AFM) was performed for the surface morphology and RMS roughness. Field-effect-transistors (FETs) were employed for mobility characterization (double Keithley 2450 with CGS-4 probe station; the channel with a 0.15 mm channel width and a 1.5 mm channel length was built on a SiO$_2$ p-type wafer, with 285 nm oxide and 100 nm aluminum contacts); photoluminescence (PL; Horiba) and X-ray photoelectron spectroscopy (XPS; ThermoFisher ESCALAB 250Xi) were utilized to obtain information on the ZnO composition and defects. Ultraviolet photoelectron spectroscopy (UPS; ThermoFisher ESCALAB 250Xi) measurements were conducted in an ultrahigh-vacuum chamber (10^{-10} mbar) with a helium(I) (21.2 eV) discharge lamp. The resolution was 0.1 eV. Copper tape was used to make the electrical contact. A 10.0 V bias was used to determine the low-kinetic-energy photoelectron cutoff. Scanning electron microscopy (SEM; FEI Helios 600 Nanolab Dual Beam System) was performed to investigate the surface morphology of the ZnO films and device structures.

Characterization of the PbS Solar Cells. J−V characteristics were conducted with a Keithley 2400 sourcemeter under simulated 1 Sun (1000 W m^{-2}) solar illumination generated by a Newport solar simulator. The various incident-light-intensity conditions were realized by neutral density filters. EQE measurements were performed under chopped monochromatic light, which originates from a halogen lamp, and the generated photocurrent was recorded by a lock-in amplifier. EIS measurement was conducted with a Gamry 500 potentiostat with a Gamry Framework for characterization of the impedance of the photovoltaic devices. In the photovoltage transient measurement, modulation of V_{OC} was realized by a 532 nm high-energy nanosecond laser (Minilite I, Continuum Laser Company) on

top of constant light bias with 5 ns pulse duration and 15 Hz repetition rate. The modulated V_{OC} was well controlled by tuning the intensity of the nanosecond laser to make sure that it was less than 10% of V_{OC}. The open-circuit voltage transient was recorded with a digital oscilloscope (TDS 380, Tektronix) at an input impedance of 1 MΩ, while the short-circuit transient was measured at an impedance of 50 Ω.

■ ASSOCIATED CONTENT

Ⓢ Supporting Information

The Supporting Information is available free of charge on the ACS Publications website at DOI: 10.1021/acsanm.8b01983.

> AFM images of the film surface (scan size 2 μm × 2 μm) for various deposited oxygen gas pressures, XRD patterns of the ZnO films on an ITO/glass substrate, energy levels with respect to a vacuum for the ZnO film deposited under different oxygen pressures and PbS−TBAI film, detailed PbS QD synthesis method, and UV−vis spectrum of the PbS CQDs (PDF)

■ AUTHOR INFORMATION

Corresponding Author

*E-mail: rln@physics.unc.edu. Tel: 1(919)962-7216.

ORCID ⊙

Jillian L. Dempsey: 0000-0002-9459-4166
Rene Lopez: 0000-0001-6274-066X

Author Contributions

All authors have contributed and approved the final version of the manuscript.

Notes

The authors declare no competing financial interest.

■ ACKNOWLEDGMENTS

■ REFERENCES

(1) Ip, A. H.; Thon, S. M.; Hoogland, S.; Voznyy, O.; Zhitomirsky, D.; Debnath, R.; Levina, L.; Rollny, L. R.; Carey, G. H.; Fischer, A.; Kemp, K. W.; Kramer, I. J.; Ning, Z. J.; Labelle, A. J.; Chou, K. W.; Amassian, A.; Sargent, E. H. Hybrid Passivated Colloidal Quantum Dot Solids. Nat. Nanotechnol. 2012, 7, 577−582.

(2) Tang, J.; Sargent, E. H. Infrared Colloidal Quantum Dots for Photovoltaics: Fundamentals and Recent Progress. Adv. Mater. 2011, 23, 12−29.

(3) Luther, J. M.; Law, M.; Beard, M. C.; Song, Q.; Reese, M. O.; Ellingson, R. J.; Nozik, A. J. Schottky Solar Cells Based on Colloidal Nanocrystal Films. Nano Lett. 2008, 8, 3488−3492.

(4) Chuang, C.-H. M.; Brown, P. R.; Bulović, V.; Bawendi, M. G. Improved Performance and Stability in Quantum Dot Solar Cells through Band Alignment Engineering. Nat. Mater. 2014, 13, 796−801.

(5) Steckel, J. S.; Coe-Sullivan, S.; Bulović, V.; Bawendi, M. G. 1.3 to 1.55 μm Tunable Electroluminescence from PbSe Quantum Dots Embedded within an Organic Device. Adv. Mater. 2003, 15, 1862−1866.

(6) Konstantatos, G.; Huang, C.; Levina, L.; Lu, Z.; Sargent, E. H. Efficient Infrared Electroluminescent Devices Using Solution-Processed Colloidal Quantum Dots. Adv. Funct. Mater. 2005, 15, 1865−1869.

(7) Sun, L.; Choi, J. J.; Stachnik, D.; Bartnik, A. C.; Hyun, B. R.; Malliaras, G. G.; Hanrath, T.; Wise, F. W. Bright Infrared Quantum-Dot Light-Emitting Diodes through Inter-Dot Spacing Control. Nat. Nanotechnol. 2012, 7, 369−373.

(8) Konstantatos, G.; Howard, I.; Fischer, A.; Hoogland, S.; Clifford, J.; Klem, E.; Levina, L.; Sargent, E. H. Ultrasensitive Solution-Cast Quantum Dot Photodetectors. Nature 2006, 442, 180−183.

(9) Cunningham, P. D.; Boercker, J. E.; Foos, E. E.; Lumb, M. P.; Smith, A. R.; Tischler, J. G.; Melinger, J. S. Enhanced Multiple Exciton Generation in Quasi-One-Dimensional Semiconductors. Nano Lett. 2011, 11, 3476−3481.

(10) Semonin, O. E.; Luther, J. M.; Choi, S.; Chen, H.; Gao, J.; Nozik, A. J.; Beard, M. C. Science 2011, 334, 1530−1534.

(11) Gao, J.; Luther, J. M.; Semonin, O. E.; Ellingson, R. J.; Nozik, A. J.; Beard, M. C. Quantum Dot Size Dependent J - V Characteristics in Heterojunction ZnO/PbS Quantum Dot Solar Cells. Nano Lett. 2011, 11, 1002−1008.

(12) Brown, P. R.; Kim, D.; Lunt, R. R.; Zhao, N.; Bawendi, M. G.; Grossman, J. C.; Bulović, V. Energy Level Modification in Lead Sulfide Quantum Dot Thin Films through Ligand Exchange. ACS Nano 2014, 8, 5863−5872.

(13) Lan, X.; Masala, S.; Sargent, E. H. Charge-Extraction Strategies for Colloidal Quantum Dot Photovoltaics. Nat. Mater. 2014, 13, 233−240.

(14) Xu, J.; Voznyy, O.; Liu, M.; Kirmani, A. R.; Walters, G.; Munir, R.; Abdelsamie, M.; Proppe, A. H.; Sarkar, A.; García De Arquer, F. P.; Wei, M.; Sun, B.; Liu, M.; Ouellette, O.; Quintero-Bermudez, R.; Li, J.; Fan, J.; Quan, L.; Todorovic, P.; Tan, H.; Hoogland, S.; Kelley, S. O.; Stefik, M.; Amassian, A.; Sargent, E. H. 2D Matrix Engineering for Homogeneous Quantum Dot Coupling in Photovoltaic Solids. Nat. Nanotechnol. 2018, 13, 456−462.

(15) Shi, G.; Wang, Y.; Liu, Z.; Han, L.; Liu, J.; Wang, Y.; Lu, K.; Chen, S.; Ling, X.; Li, Y.; Cheng, S.; Ma, W. Stable and Highly Efficient PbS Quantum Dot Tandem Solar Cells Employing a Rationally Designed Recombination Layer. Adv. Energy Mater. 2017, 7, 1602667.

(16) Lan, X.; Voznyy, O.; Kiani, A.; García De Arquer, F. P.; Abbas, A. S.; Kim, G. H.; Liu, M.; Yang, Z.; Walters, G.; Xu, J.; Yuan, M.; Ning, Z.; Fan, F.; Kanjanaboos, P.; Kramer, I.; Zhitomirsky, D.; Lee, P.; Perelgut, A.; Hoogland, S.; Sargent, E. H. Passivation Using Molecular Halides Increases Quantum Dot Solar Cell Performance. Adv. Mater. 2016, 28, 299−304.

(17) Liu, M.; De Arquer, F. P. G.; Li, Y.; Lan, X.; Kim, G. H.; Voznyy, O.; Jagadamma, L. K.; Abbas, A. S.; Hoogland, S.; Lu, Z.; Kim, J. Y.; Amassian, A.; Sargent, E. H. Double-Sided Junctions Enable High-Performance Colloidal-Quantum-Dot Photovoltaics. Adv. Mater. 2016, 28, 4142−4148.

(18) Luo, J.; Dai, X.; Bai, S.; Jin, Y.; Ye, Z.; Guo, X. Ligand Exchange of Colloidal ZnO Nanocrystals from the High Temperature and Nonaqueous Approach. Nano-Micro Lett. 2013, 5, 274−280.

(19) Janotti, A.; Van De Walle, C. G. Fundamentals of Zinc Oxide as a Semiconductor. Rep. Prog. Phys. 2009, 72, 126501.

(20) Singh, K. J.; Singh, C. A.; Singh, T. J.; Chettri, D.; Sarkar, S. K. ZnO Based Homojunction P-i-n Solar Cell to Self-Power UV Detector. Proc. Int. Conf. Inven. Commun. Comput. Technol. 2017, 304−307.

(21) Kim, G. H.; García De Arquer, F. P.; Yoon, Y. J.; Lan, X.; Liu, M.; Voznyy, O.; Yang, Z.; Fan, F.; Ip, A. H.; Kanjanaboos, P.; Hoogland, S.; Kim, J. Y.; Sargent, E. H. High-Efficiency Colloidal Quantum Dot Photovoltaics via Robust Self-Assembled Monolayers. Nano Lett. 2015, 15, 7691−7696.

(22) Yang, Z.; Janmohamed, A.; Lan, X.; García De Arquer, F. P.; Voznyy, O.; Yassitepe, E.; Kim, G. H.; Ning, Z.; Gong, X.; Comin, R.; Sargent, E. H. Colloidal Quantum Dot Photovoltaics Enhanced by Perovskite Shelling. *Nano Lett.* **2015**, *15*, 7539−7543.

(23) Yang, X.; Hu, L.; Deng, H.; Qiao, K.; Hu, C.; Liu, Z.; Yuan, S.; Khan, J.; Li, D.; Tang, J.; Song, H.; Cheng, C. Improving the Performance of PbS Quantum Dot Solar Cells by Optimizing ZnO Window Layer. *Nano-Micro Lett.* **2017**, *9*, 1−10.

(24) Rekemeyer, P. H.; Chang, S.; Chuang, C. H. M.; Hwang, G. W.; Bawendi, M. G.; Gradečak, S. Enhanced Photocurrent in PbS Quantum Dot Photovoltaics via ZnO Nanowires and Band Alignment Engineering. *Adv. Energy Mater.* **2016**, *6*, 1600848.

(25) Jean, J.; Chang, S.; Brown, P. R.; Cheng, J. J.; Rekemeyer, P. H.; Bawendi, M. G.; Gradečak, S.; Bulović, V. ZnO Nanowire Arrays for Enhanced Photocurrent in PbS Quantum Dot Solar Cells. *Adv. Mater.* **2013**, *25*, 2790−2796.

(26) Bai, S.; Wu, Z.; Xu, X.; Jin, Y.; Sun, B.; Guo, X.; He, S.; Wang, X.; Ye, Z.; Wei, H.; Han, X.; Ma, W. Inverted Organic Solar Cells Based on Aqueous Processed ZnO Interlayers at Low Temperature. *Appl. Phys. Lett.* **2012**, *100*, 203906.

(27) Jagadamma, L. K.; Abdelsamie, M.; El Labban, A.; Aresu, E.; Ngongang Ndjawa, G. O.; Anjum, D. H.; Cha, D.; Beaujuge, P. M.; Amassian, A. Efficient Inverted Bulk-Heterojunction Solar Cells from Low-Temperature Processing of Amorphous ZnO Buffer Layers. *J. Mater. Chem. A* **2014**, *2*, 13321−13331.

(28) You, J.; Chen, C. C.; Dou, L.; Murase, S.; Duan, H. S.; Hawks, S. A.; Xu, T.; Son, H. J.; Yu, L.; Li, G.; Yang, Y. Metal Oxide Nanoparticles as an Electron-Transport Layer in High-Performance and Stable Inverted Polymer Solar Cells. *Adv. Mater.* **2012**, *24*, 5267−5272.

(29) Choopun, S.; Vispute, R. D.; Noch, W.; Balsamo, A.; Sharma, R. P.; Venkatesan, T.; Iliadis, A.; Look, D. C. *Appl. Phys. Lett.* **1999**, *75*, 3947−3949.

(30) Christoulakis, S.; Suchea, M.; Koudoumas, E.; Katharakis, M.; Katsarakis, N.; Kiriakidis, G. Thickness Influence on Surface Morphology and Ozone Sensing Properties of Nanostructured ZnO Transparent Thin Films Grown by PLD. *Appl. Surf. Sci.* **2006**, *252*, 5351−5354.

(31) Garvey, T. R.; Farnum, B. H.; Lopez, R. Pulsed Laser Deposited Porous Nano-Carpets of Indium Tin Oxide and Their Use as Charge Collectors in Core-Shell Structures for Dye Sensitized Solar Cells. *Nanoscale* **2015**, *7*, 2400−2408.

(32) Cullity, B. D. *Elements of Diffraction*, 2nd ed.; Addison-Wesley Publishing Company, Inc.,1978; Chapter 3, pp 101−103.

(33) Yang, D.; Li, B.; Hu, C.; Deng, H.; Dong, D.; Yang, X.; Qiao, K.; Yuan, S.; Song, H. Controllable Growth Orientation of SnS$_2$ Flakes for Low-Noise, High-Photoswitching Ratio, and Ultrafast Phototransistors. *Adv. Opt. Mater.* **2016**, *4*, 419−426.

(34) Cowan, S. R.; Roy, A.; Heeger, A. J. Recombination in Polymer-Fullerene Bulk Heterojunction Solar Cells. *Phys. Rev. B: Condens. Matter Mater. Phys.* **2010**, *82*, 245207.

(35) Gadisa, A.; Hara, Y.; Fu, Y.; Vrouwenvelder, K. T.; Dempsey, J. L.; Samulski, E. T.; Lopez, R. Disparity in Optical Charge Generation and Recombination Processes in Upright and Inverted PbS Quantum-Dot Solar Cells. *J. Phys. Chem. C* **2015**, *119*, 4606−4611.

(36) Hara, Y.; Gadisa, A.; Fu, Y.; Garvey, T.; Vrouwenvelder, K. T.; Miller, C. W.; Dempsey, J. L.; Lopez, R. Gains and Losses in PbS Quantum Dot Solar Cells with Submicron Periodic Grating Structures. *J. Phys. Chem. C* **2016**, *120*, 8005−8013.

(37) Mallajosyula, A. T.; Iyer, S. S. K.; Mazhari, B. Charge Transport in Polythiophene:Fullerene:Nanotube Bulk Heterojunction Photovoltaic Devices Investigated by Impedance Spectroscopy. *Curr. Appl. Phys.* **2013**, *13*, 677−683.

(38) Wang, H.; Wang, Y.; He, B.; Li, W.; Sulaman, M.; Xu, J.; Yang, S.; Tang, Y.; Zou, B. Charge Carrier Conduction Mechanism in PbS Quantum Dot Solar Cells: Electrochemical Impedance Spectroscopy Study. *ACS Appl. Mater. Interfaces* **2016**, *8*, 18526−18533.

(39) Bisquert, J. Theory of the Impedance of Electron Diffusion and Recombination in a Thin Layer. *J. Phys. Chem. B* **2002**, *106*, 325−333.

(40) Mora-Seró, I.; Garcia-Belmonte, G.; Boix, P. P.; Vázquez, M. A.; Bisquert, J. Impedance Spectroscopy Characterisation of Highly Efficient Silicon Solar Cells under Different Light Illumination Intensities. *Energy Environ. Sci.* **2009**, *2*, 678−686.

(41) Moehl, T.; Kytin, V. G.; Bisquert, J.; Kunst, M.; Bolink, H. J.; Garcia-Belmonte, G. Relaxation of Photogenerated Carriers in P3HT:PCBM Organic Blends. *ChemSusChem* **2009**, *2*, 314−320.

(42) Mora-Seró, I.; Luo, Y.; Garcia-Belmonte, G.; Bisquert, J.; Muñoz, D.; Voz, C.; Puigdollers, J.; Alcubilla, R. Recombination Rates in Heterojunction Silicon Solar Cells Analyzed by Impedance Spectroscopy at Forward Bias and under Illumination. *Sol. Energy Mater. Sol. Cells* **2008**, *92*, 505−509.

(43) Shuttle, C. G.; O'Regan, B.; Ballantyne, A. M.; Nelson, J.; Bradley, D. D. C.; De Mello, J.; Durrant, J. R. Experimental Determination of the Rate Law for Charge Carrier Decay in a Polythiophene: Fullerene Solar Cell. *Appl. Phys. Lett.* **2008**, *92*, 093311.

(44) O'Regan, B. C.; Scully, S.; Mayer, A. C.; Palomares, E.; Durrant, J. The Effect of Al$_2$O$_3$ Barrier Layers in TiO$_2$/Dye/CuSCN Photovoltage Cells Explored by Recombination and DOS Characterization Using Transient Photovoltage Measurements. *J. Phys. Chem. B* **2005**, *109*, 4616−4623.

(45) Prasada Rao, T.; Goswami, G. K.; Nanda, K. K. Detailed Understanding of the Excitation-Intensity Dependent Photoluminescence of ZnO Materials: Role of Defects. *J. Appl. Phys.* **2014**, *115*, 213513.

(46) Chen, S.; Small, C. E.; Amb, C. M.; Subbiah, J.; Lai, T. H.; Tsang, S. W.; Manders, J. R.; Reynolds, J. R.; So, F. Inverted Polymer Solar Cells with Reduced Interface Recombination. *Adv. Energy Mater.* **2012**, *2*, 1333−1337.

(47) Zeng, H.; Duan, G.; Li, Y.; Yang, S.; Xu, X.; Cai, W. Blue Luminescence of ZnO Nanoparticles Based on Non-Equilibrium Processes: Defect Origins and Emission Controls. *Adv. Funct. Mater.* **2010**, *20*, 561−572.

(48) Sun, Y.; Seo, J. H.; Takacs, C. J.; Seifter, J.; Heeger, A. J. Inverted Polymer Solar Cells Integrated with a Low-Temperature-Annealed Sol-Gel-Derived ZnO Film as an Electron Transport Layer. *Adv. Mater.* **2011**, *23*, 1679−1683.

(49) Hines, M. A.; Scholes, G. D. Colloidal PbS Nanocrystals with Size-Tunable Near-Infrared Emission: Observation of Post-Synthesis Self-Narrowing of the Particle Size Distribution. *Adv. Mater.* **2003**, *15*, 1844−1849.

(50) Moreels, I.; Lambert, K.; Smeets, D.; De Muynck, D.; Nollet, T.; Martins, J. C.; Vanhaecke, F.; Vantomme, A.; Delerue, C.; Allan, G.; Hens, Z. Size-Dependent Optical Properties of Colloidal PbS Quantum Dots. *ACS Nano* **2009**, *3*, 3023−3030.

(51) Kessler, M. L.; Starr, H. E.; Knauf, R. R.; Rountree, K. J.; Dempsey, J. L. Exchange equilibria of carboxylate-terminated ligands at PbS nanocrystal surfaces. *Phys. Chem. Chem. Phys.* **2018**, *20*, 23649−23655.